

VIP Very Important Paper

www.batteries-supercaps.org

Block Copolymer-Derived Porous Carbon Fibers Enable High MnO₂ Loading and Fast Charging in Aqueous Zinc-Ion Battery

Dong Guo,^[a] Wenqi Zhao,^[a] Fuping Pan,^[a] and Guoliang Liu^{*[a, b, c]}

Rechargeable aqueous Zn–MnO₂ batteries are promising for stationary energy storage because of their high energy density, safety, environmental benignity, and low cost. Conventional gravel MnO₂ cathodes have low electrical conductivity, slow ion (de-)insertion, and poor cycle stability, resulting in poor recharging performance and severe capacity fading. To improve the rechargeability of MnO₂, strategies have been devised such as depositing micrometer-thick MnO₂ on carbon cloth and blending nanostructured MnO₂ with additives and binders. The low electrical conductivity of binders and sluggish ion (de-)insertion in micrometer-thick MnO₂, however, still limit the fast-charging performance. Herein, we have prepared porous carbon

fiber (PCF) supported MnO₂ cathodes (PCF@MnO₂), comprised of nanometer-thick MnO₂ uniformly deposited on electrospun block copolymer-derived PCF that have abundant uniform mesopores. The high electrical conductivity of PCF, fast electrochemical reactions in nanometer-thick MnO₂, and fast ion transport through porous nonwoven fibers contribute to a high rate capability at high loadings. PCF@MnO₂, at a MnO₂ loading of 59.1 wt %, achieves a MnO₂-based specific capacity of 326 and 184 mAh g⁻¹ at a current density of 0.1 and 1.0 Ag⁻¹, respectively. Our approach of block copolymer-based PCF as a support for zinc-ion cathode inspires future designs of fast-charging electrodes with other active materials.

Introduction

Reliable energy supports the prosperity of human society since time immemorial.^[1,2] Lithium-ion batteries dominate the secondary energy storage nowadays, but the scarcity and uneven distribution of lithium in Earth's crust, as well as the potential fire hazard, still draw concerns.^[3–5] Rechargeable aqueous zinc-ion battery (ZIB) is promising for highly demanding stationary energy storage owing to the abundant zinc reserve, non-flammable aqueous electrolyte, high energy density, environmental friendliness, and low cost.^[1,3–15] The development of fast-charging cathodes for ZIBs, however, remains a challenge.^[3,4,8,9,14,16] Pioneered by Georges Leclanché in his design of Zn–MnO₂ cell since 1860s,^[17] MnO₂ has been the primary cathode material in ZIBs due to its high voltage vs. Zn/ Zn^{2+}

Zn²⁺ and the aforementioned traits.^[12,18–23] However, the low electrical conductivity and slow ion (de-)insertion of micro-meter-sized MnO₂ gravels result in poor recharging performance.^[19,24] Furthermore, the bulky MnO₂ gravels are susceptible to capacity fading due to low tolerance to cycling-induced volume expansion and Mn²⁺ dissolution,^[25–30] limiting the rechargeability.

To overcome the limitations of monolithic MnO₂ gravels, MnO₂ has been structurally engineered as nanorods,^[8,22,26,29,31] nanosheets^[20,32–34] and nanospheres^[35–40] via hydrothermal reactions. The nanostructured MnO₂ to some extent improves the kinetics of ion (de-)insertion.^[8,20,26,29,31–39] However, the discrete MnO₂ nanoparticles rely on conductive additives (such as acetylene black, 15–25 wt %) and binders (i.e., PVDF, 10–15 wt %) to construct electrically conductive cathodes,^[20,26,32,35] yet the inadequate overall conductivity hinders fast charging especially at high current densities.^[26,32,41] Disparately, electro-depositing MnO₂ on carbon cloth yields highly conductive cathodes thanks to the continuous graphitic carbon matrix.^[9,42–45] Due to the limited surface area, however, high mass loading and low thickness of MnO₂ on carbon cloth are mutually exclusive.^[9,42–45] Therefore, it is imperative to develop electrically conductive electrodes with high MnO₂ loadings while simultaneously maintaining the MnO₂ nanostructures to ensure fast charging.

Herein, we report a judiciously designed fast-charging electrode of porous carbon fiber (PCF) supported MnO₂ (PCF@MnO₂). Nanometer-thick MnO₂ is deposited on block copolymer-derived PCF. The graphitic PCF provides high electrical conductivity. Additionally, the internal uniform mesopores, defined by block copolymer microphase separation, offer a high surface area and enable a high loading of MnO₂.

[a] D. Guo, W. Zhao, F. Pan, Prof. G. Liu

Department of Chemistry
Virginia Tech
Blacksburg, VA 24061, USA
E-mail: gliu1@vt.edu[b] Prof. G. Liu
Macromolecules Innovation Institute
Virginia Tech
Blacksburg, VA 24061, USA[c] Prof. G. Liu
Division of Nanoscience, Academy of Integrated Science
Virginia Tech
Blacksburg, VA 24061, USA
 Supporting information for this article is available on the WWW under <https://doi.org/10.1002/batt.202100380>
 © 2022 The Authors. *Batteries & Supercaps* published by Wiley-VCH GmbH. This is an open access article under the terms of the Creative Commons Attribution Non-Commercial NoDerivs License, which permits use and distribution in any medium, provided the original work is properly cited, the use is non-commercial and no modifications or adaptations are made.

Systematic investigations into the kinetics of MnO_2 deposition suggest that room temperature (RT) incubation of PCF in KMnO_4 solutions favors uniform in-mesopore deposition of thin MnO_2 . Benefiting from the synergistically combined advantages of good electrical conductivity, fast ion transport, and fast electrochemical reactions in thin MnO_2 , the resulting PCF@ MnO_2 containing 59.1 wt% of MnO_2 exhibits a high MnO_2 -based capacity of 326 and 184 mAh g^{-1} at a current density of 0.1 and 1.0 A g^{-1} , respectively, as well as outstanding specific power/energy densities.

Results and Discussion

Fast charging requires high electrical conductivity, swift ion transport, and prompt electrochemical reactions in the electrode. PCF@ MnO_2 meets these criteria because i) PCF has high electrical conductivity, ii) the porous fibrous network allows for fast ion transport, and iii) the uniform thin MnO_2 affords fast electrochemical reactions (Figure 1a). Importantly, PCF has highly uniform mesopores to enable high loadings of MnO_2 in the cathode. In this work, PCF mats were prepared by electrospinning, microphase separation, and pyrolysis of block copolymer poly(methyl methacrylate)-block-polyacrylonitrile (PMMA-*b*-PAN) fibers. Synthesized via reversible addition-fragmentation chain-transfer (RAFT) polymerization,^[45–47] PMMA-*b*-PAN had a number-average molecular weight (M_n) of 56-*b*-76 kDa, giving a PMMA weight fraction (Φ_{PMMA}) of 42% (Figures 1b, d and S1).

After electrospinning and pyrolysis, PAN was converted to carbon, and PMMA was decomposed to create mesopores. The PCF exhibited a median mesopore width of ~12 nm (Figure 1e) with a high specific surface area of 537 $\text{m}^2 \text{g}^{-1}$ (Figure S2).

The high surface area facilitated the subsequent MnO_2 deposition via incubation in KMnO_4 solutions involving the follow chemical reaction.^[45]



MnO_2 was produced from the redox reaction between KMnO_4 and carbon on the interface of aqueous KMnO_4 solution and PCF. KMnO_4 served as the source of Mn. In this redox reaction, the oxidation state of Mn in KMnO_4 reduced to produce MnO_2 . Meanwhile, a small amount of carbon on the interface was oxidized. The resulting MnO_2 was not soluble in the aqueous medium, thus being deposited on PCF. The MnO_2 was primarily in the form of $\delta\text{-MnO}_2$ (Figure S3). To examine the effects of incubation on MnO_2 deposition, we prepared PCF@ MnO_2 under two conditions: 1) in a 10 mM KMnO_4 solution at 80 °C for up to 120 min and 2) in a 63 mM KMnO_4 solution at room temperature (RT) for up to 48 hours. The resulting PCF@ MnO_2 were characterized using scanning electron microscopy (SEM) (Figure 2). PCF@ MnO_2 incubated at 80 °C displayed petal-like MnO_2 nanosheets on the fiber surface, because in an oxidation-intercalation-exfoliation process,^[48] carbon sheets exfoliated from PCF and MnO_2 was deposited on the exposed carbon sheets. As incubation time was increased,

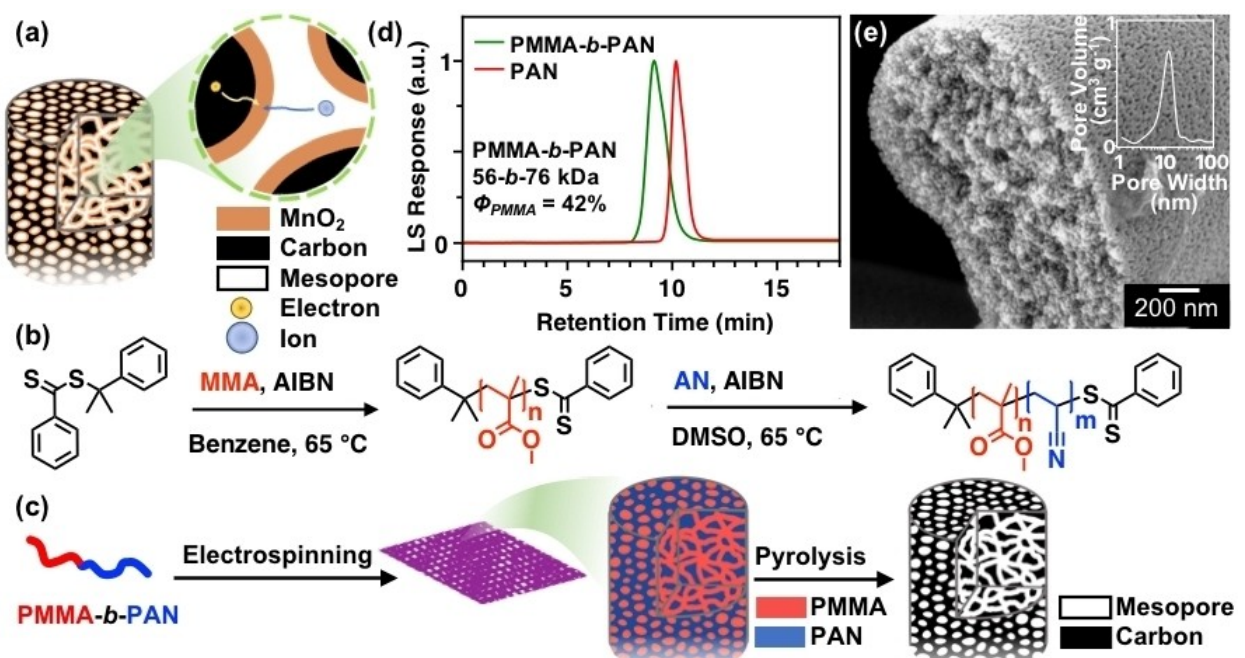


Figure 1. Preparation of PCF and PCF@ MnO_2 cathodes. a) Design of high-loading fast-charging PCF@ MnO_2 cathode using PCF with uniform mesopores. The high surface area of internal mesopores in PCF affords a high loading of nanometer-thick MnO_2 , which minimizes the ion (de-)insertion length to achieve fast charging. The continuous fiber provides highly conductive pathways for electrons to ensure fast charging. b) Synthesis of PMMA-*b*-PAN as a PCF precursor. c) Preparation of PCF. PMMA-*b*-PAN was electrospun into a mat of block copolymer fibers. The zoomed-in view shows that block copolymer fibers undergo microphase separation to form uniform nanoscale domains and pyrolysis to form mesoporous carbon structures. d) Size exclusion chromatography (SEC) traces of PMMA-*b*-PAN and PMMA using a light scattering (LS) detector. e) Representative cross-sectional SEM image of PCF shows mesopores uniformly distributed in the fiber. The inset shows the pore size distribution with a median pore width of 12 nm, as determined by gas sorption.

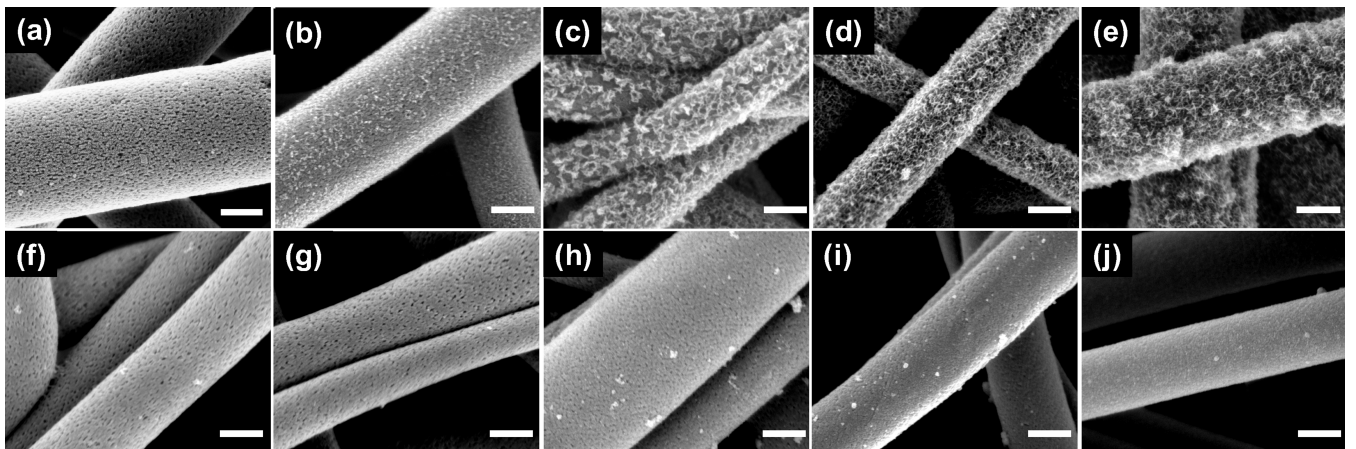


Figure 2. Morphologies of PCF@MnO₂ cathodes. PCF@MnO₂ cathodes were prepared by incubating a) pristine PCF in an aqueous solution of 10 mM KMnO₄ at 80 °C for b) 15 min, c) 30 min, d) 60 min, and e) 120 min or incubating PCF in an aqueous solution of 63 mM KMnO₄ at RT for f) 3 h, g) 6 h, h) 12 h, i) 24 h, and j) 48 h, respectively. Scale bars, 300 nm.

the size and areal density of MnO₂ petals increased. As incubation time was further increased, the redox reaction consumed the exfoliated carbon sheets, resulting in discontinuous carbon detached from PCF and a large amount of MnO₂ deposited outside the mesopores (Figure 2a–e). Conversely, the incubation at RT maintained intact PCF and thin MnO₂ layers uniformly deposited on both internal and external surfaces of PCF (Figure 2f–j). As a result, the mesopore widths decreased, confirming that MnO₂ filled in mesopores. To highlight the importance of mesopores, carbon fibers (CF) containing no mesopores were also incubated under similar conditions. CF incubated at 80 °C underwent a surface exfoliation and thus displayed similar petal-like MnO₂ sheets (Figure 3a–e). Whereas the incubation of CF at RT yielded uniform thin MnO₂ layer on CF surface (Figure 3f–j).

The mass loadings of MnO₂, Φ_{MnO_2} , after varying incubation time was calculated using Equation (1).^[45]

$$\Phi_{\text{MnO}_2} = \frac{(m_{\text{PCF@MnO}_2} - m_{\text{PCF}}) \times 4M_{\text{MnO}_2}}{m_{\text{PCF@MnO}_2} \times (4M_{\text{MnO}_2} - 3M_{\text{C}})} \quad (1)$$

where $m_{\text{PCF@MnO}_2}$ and m_{PCF} are the masses of PCF@MnO₂ and PCF mats, respectively. M_{MnO_2} and M_{C} are the molar mass of MnO₂ and carbon, 86.9 and 12.0 g mol⁻¹, respectively. As summarized in Table 1 and Figure 4(a and b), Φ_{MnO_2} increased with incubation time under both conditions. As expected, a higher incubation temperature at 80 °C enabled faster MnO₂ deposition than RT. After incubating at 80 °C for 120 min, Φ_{MnO_2} attained 71.2%, almost comparable to MnO₂ loadings in cathodes prepared using MnO₂ powders, conductive additives, and binders.^[20,26,32,35] The incubation at RT exhibited slow kinetics, but the PCF@MnO₂ still reached a high Φ_{MnO_2} of 59.1% after 48 h, approaching the MnO₂ loading in powder-additive-binder based cathodes.

The in-mesopore nanometer-thick MnO₂ is imperative for fast charging because it has a large electrolyte/electrode

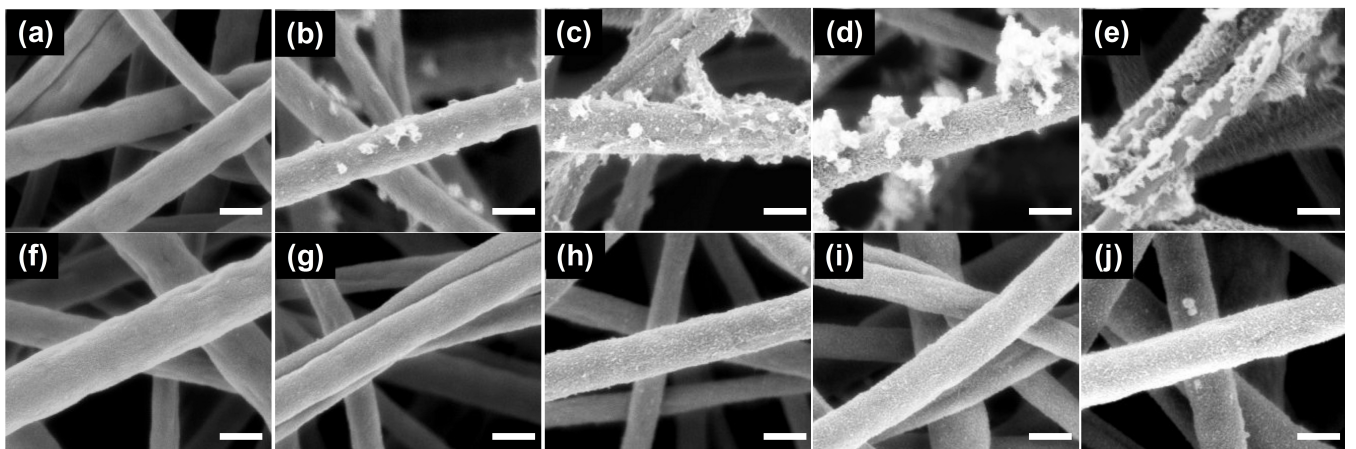


Figure 3. Morphologies of CF@MnO₂. CF@MnO₂ were prepared by incubating a) CF in a 10 mM KMnO₄ aqueous solution at 80 °C for b) 15 min, c) 30 min, d) 60 min, and e) 120 min or incubating CF in a 63 mM KMnO₄ solution at RT for f) 3 h, g) 6 h, h) 12 h, i) 24 h, and j) 48 hours, respectively. Scale bars, 300 nm.

Table 1. Mass loadings of MnO₂ in PCF@MnO₂ and CF@MnO₂.

Incubation condition	Time	Φ_{MnO_2} of PCF@MnO ₂ [%]	$S_{\text{MnO}_2} [\text{mg cm}^{-2}]^{\text{[a]}}$	Φ_{MnO_2} of CF@MnO ₂ [%]	Φ_{mesopore} of PCF@MnO ₂ [%]
10 mM KMnO ₄ at 80 °C	15 min	34.6	1.66	9.69	79.7
	30 min	42.7	2.29	18.5	69.6
	60 min	55.9	3.71	32.3	62.2
	120 min	71.2	6.53	53.4	53.6
63 mM KMnO ₄ at RT	3 h	23.7	1.00	4.05	86.5
	6 h	31.0	1.42	6.57	84.4
	12 h	40.9	2.14	11.6	81.0
	24 h	50.2	3.02	18.1	78.0
	48 h	59.1	4.16	25.7	76.0

[a] Areal MnO₂ loading of PCF@MnO₂.

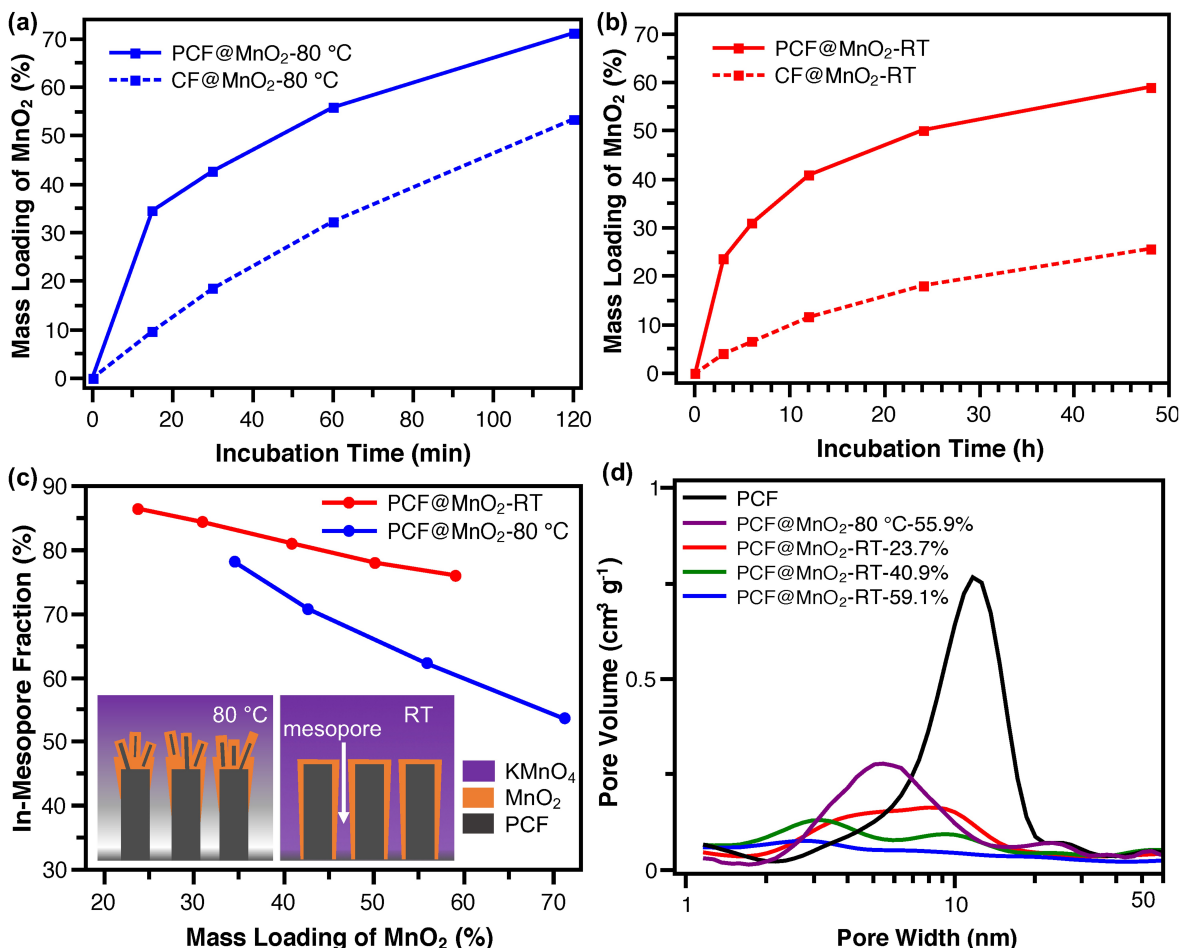


Figure 4. Mass loadings of MnO₂ (Φ_{MnO_2}) in PCF@MnO₂ and CF@MnO₂ incubated at a) 80 °C and b) RT. c) The in-mesopore fraction of MnO₂ (Φ_{mesopore}) decreased at higher Φ_{MnO_2} . Incubation at RT favors higher Φ_{mesopore} . The insets show the carbon exfoliation and KMnO₄ depletion at 80 °C resulted in less in-mesopore MnO₂, whereas RT-incubation uniformly deposited MnO₂ both inside and outside mesopores. d) Pore size distribution confirms that pore widths decreased at higher Φ_{MnO_2} due to MnO₂ filling in mesopores. Incubation at RT yields more MnO₂ deposition in the mesopores than at 80 °C.

interface and short ion diffusion path.^[9] To estimate the fraction of in-mesopore MnO₂, PCF@MnO₂ was compared against the corresponding CF@MnO₂ (Table 1, Figure 4a and b). The CF@MnO₂ had a smaller Φ_{MnO_2} than the corresponding PCF@MnO₂ because CF had no mesopores. The disparity of Φ_{MnO_2} between CF@MnO₂ and PCF@MnO₂ provides a means to estimate the in-mesopore fraction of MnO₂, Φ_{mesopore} , using Equation (2).

$$\Phi_{\text{mesopore}} = \frac{(m_{\text{PCF@MnO}_2} - m_{\text{PCF}}) - (m_{\text{CF@MnO}_2} - m_{\text{CF}})}{m_{\text{PCF@MnO}_2} - m_{\text{PCF}}} \quad (2)$$

where $m_{\text{PCF@MnO}_2}$, m_{PCF} , $m_{\text{CF@MnO}_2}$ and m_{CF} are the masses of PCF@MnO₂, PCF, CF@MnO₂ and CF mats, respectively. PCF@MnO₂ incubated at RT displayed a higher Φ_{mesopore} than the counterpart incubated at 80 °C at the same overall loading of MnO₂ (Figure 4c), owing to two reasons. First, the slow

incubation reaction at RT and high KMnO_4 concentration avoided the depletion of KMnO_4 in the mesopores. Second, the RT-incubation minimized the surface exfoliation of PCF occurring at high temperatures, thus almost no petal-like MnO_2 appeared on PCF surfaces (Figure 2). The in-mesopore deposition of MnO_2 was further confirmed by the pore size reduction of PCF@ MnO_2 , as characterized using nitrogen sorption (Figures 4d, S2). The median mesopore size of pristine PCF was 11.7 nm. As Φ_{MnO_2} increased from 23.7% to 40.9% and to 59.1% (denoted as PCF@ MnO_2 RT-23.7%, -40.9% and -59.1%), the pore width decreased from 9.3 to 3.4 and to 2.9 nm, indicating increasing in-mesopore MnO_2 deposition of 1.2, 4.2, and 4.4-nm-thick, respectively, and concurring the observation under SEM (Figure 2f-j). Importantly, PCF@ MnO_2 incubated at 80 °C with a Φ_{MnO_2} of 55.9% (denoted as PCF@ MnO_2 80 °C-55.9%) displayed a larger pore width of 5.4 nm than the 2.9 nm for the counterpart at RT with a Φ_{MnO_2} of 59.1% (PCF@ MnO_2 RT-59.1%), further consolidating that the incubation at RT allowed more in-mesopore deposition of MnO_2 and held greater promise for producing fast-charging electrodes.

The electrochemical kinetics of PCF@ MnO_2 was investigated using cyclic voltammetry (Figures 5a, b and S4). PCF@ MnO_2 80 °C-55.9% and RT-59.1% exemplified the current-voltage profiles at different scan rates, exhibiting two oxidative peaks (Peak 1 near 1.56 V, Peak 2 near 1.61 V) and two reductive peaks (Peak 3 near 1.37, Peak 4 near 1.23 V) due to the debatable two-regime electrochemical reactions reported in the literature.^[8,9,49,50] Usually the peak currents, i , scales with scan rates, v , following the relationship $i = av^b$, where a is a constant and the exponent b is indicative of the electrochemical kinetics to be battery-like or capacitor-like.^[51] An ideal battery has a b value of 0.5 and an ideal capacitor displays $b = 1$.^[51,52] Peak 1 showed b values of 0.56 and 0.55 for PCF@ MnO_2 80 °C-55.9% and RT-59.1%, respectively, suggesting dominantly battery-like energy storage (Figure 5c and d). Peak 2 exhibited b values of 0.70 and 0.69 for PCF@ MnO_2 80 °C-55.9% and RT-59.1%, respectively, implying combined behaviors of battery and capacitor. Peak 3 and 4, as the reversed reactions of Peak 2 and 1, respectively, presented similar kinetics during discharging.

To further decouple the capacitive and diffusion-controlled contributions, the currents at varying scan rates from 0.1 to 0.5 mV s⁻¹ were analyzed using Equation (3).^[53]

$$i = k_1v + k_2v^{0.5} \quad (3)$$

where k_1, k_2 are constants, k_1v represents the capacitive contribution and $k_2v^{0.5}$ is the diffusion-controlled contribution.^[53] The decoupled currents displayed total capacitive contributions in the range of 53%–75% for PCF@ MnO_2 80 °C-55.9%, and 49%–69% for PCF@ MnO_2 RT-59.1% (Figure 5e and f). The capacitive contributions for PCF@ MnO_2 80 °C-55.9% were in general slightly higher than PCF@ MnO_2 RT-59.1%, presumably due to two reasons: i) PCF@ MnO_2 80 °C-55.9% has a higher specific surface area than PCF@ MnO_2 RT-59.1%, resulting from less in-mesopore MnO_2 deposition (Figure S2).

The higher surface area of PCF@ MnO_2 80 °C-55.9% resulted in more ion storage on surfaces. ii) The uniform MnO_2 thin layer and good electrical conductivity of PCF in PCF@ MnO_2 RT-59.1% better facilitated the diffusion-controlled ion (de-)insertion.

The fast charging of PCF@ MnO_2 cathodes was evaluated using rate capability at increasing current densities. PCF@ MnO_2 80 °C-55.9%, RT-59.1% (Figure 6a, b) and all other cathodes (Figure S5) exhibited a two-stage discharging voltage profile because of the two-regime mechanism.^[8,9,49] As the current density increased from 0.1 to 6.0 A g⁻¹, all PCF@ MnO_2 cathodes showed decreasing MnO_2 -based specific capacities because fast charging rates retarded the cathodic reactions. PCF@ MnO_2 cathodes with higher Φ_{MnO_2} displayed lower rate capabilities, because thicker MnO_2 layers hindered electron conduction and slowed down ion (de-)insertion (Figure 6c and d). After charging at 6.0 A g⁻¹, all PCF@ MnO_2 cathodes were cycled at 0.1 A g⁻¹ again. The recovered capacities indicated good structural stability of PCF@ MnO_2 at various current densities.

The RT-incubated PCF@ MnO_2 cathodes showed better rate capability than the 80 °C-incubated analogues at similar Φ_{MnO_2} , confirming that the uniform thin-layer MnO_2 on PCF benefited better fast charging than the petal-like MnO_2 sheet on exfoliated PCF (Figure 6e). The long-term cycle stability of PCF@ MnO_2 is also expected to improve because the PCF supported thin-layer MnO_2 can better tolerate volume expansion. Furthermore, the mesopores confine the potentially dissolved Mn^{2+} and enable better MnO_2 recovery during cycling.^[25–30] After initial charging at 0.1 A g⁻¹ for 5 cycles, PCF@ MnO_2 80 °C-55.9% and RT-59.1% were repeatedly charged at a current density of 1.0 A g⁻¹. PCF@ MnO_2 80 °C-55.9% and RT-59.1% both displayed stable specific capacities for 500 cycles (Figure 6f). The slight increase in specific capacity after 50 cycles is presumably resulted from the electric activation and recovered Mn^{2+} additives.^[9,25,29,50,54] The areal loading of MnO_2 significantly altered the energy density and power density. The RT-incubated PCF@ MnO_2 with areal MnO_2 loadings of 1.00 and 1.42 mg cm⁻² showed leading MnO_2 -based energy and power densities (Figure 6g). An MnO_2 areal loading of ~2 mg cm⁻² is widely employed in cathodes consisting of nanostructured MnO_2 , conductive additives and binders.^[6,20] PCF@ MnO_2 with a MnO_2 loading of 2.14 mg cm⁻² exhibited comparable energy and power densities with graphene scroll-coated $\alpha\text{-MnO}_2$ nanowires,^[26] implying the good electrical conductivity of graphitic PCF and graphene is crucial for fast charging. Even at high loadings of 3.06 and 4.16 mg cm⁻², PCF@ MnO_2 retained high energy and power densities comparable to $\alpha\text{-MnO}_2$ and $\beta\text{-MnO}_2$ cathodes that were at a much lower MnO_2 loading of ~2 mg cm⁻².

Our RT-incubated PCF@ MnO_2 cathodes exhibit outstanding fast-charging performance at high mass loadings in aqueous zinc-ion batteries. The PCF@ MnO_2 cathodes embrace following attributes: 1) good electrical conductivity of PCF, 2) fast ion (de-)insertion in nanometer-thick MnO_2 , and 3) fast ion transport in the porous nonwoven cathodic structure. Based on the findings herein, we propose that future designs of superior fast-charging MnO_2 -based cathodes must fulfill the following characteristics. First, MnO_2 should be in the form of low-

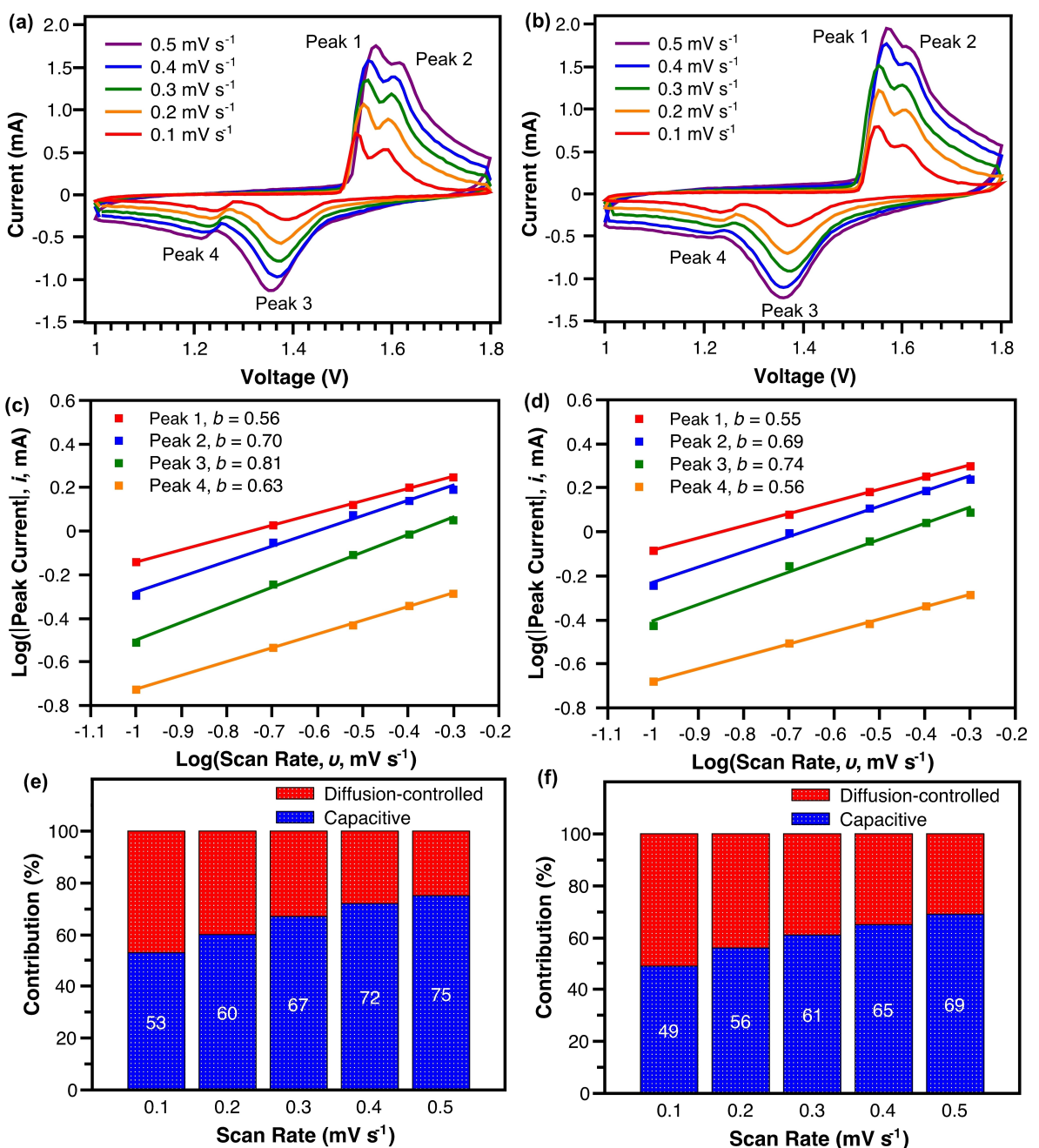


Figure 5. Kinetic analysis of PCF@MnO₂. a, b) Cyclic voltammograms, c, d) metric b of peak currents, and e, f) capacitive contributions of a, c, e) PCF@MnO₂ 80 °C-55.9% and b, d, f) PCF@MnO₂ RT-59.1%.

dimension nanostructures, preferably nanometer-thick layers. The low-dimension MnO₂ promotes fast ion (de-)insertion by increasing the electrode/electrolyte interface and shortening the ion diffusion path.^[9,20,32-34] Additionally, the low-dimension MnO₂ within confined spaces enables long-term cycle stability because of the tolerance to volume expansion and the ability to recover dissolved Mn²⁺.^[25-30] Second, fast-charging cathodes demand good electrical conductivity. Intimate MnO₂/matrices contact and highly electroconductive matrices (e.g., graphitic carbon fibers and graphene) are essential to ensure good electrical conductivity.^[26] Third, a porous network benefits fast

charging because of easy electrolyte infiltration and fast ion transport. With internal mesopores molecularly defined by block copolymers, the porous nonwoven fibrous structure from electrospinning is highly effective in high loading and fast charging.

Conclusion

In summary, we have prepared PCF@MnO₂ consisting of nanometer-thick MnO₂ deposited on block copolymer-derived

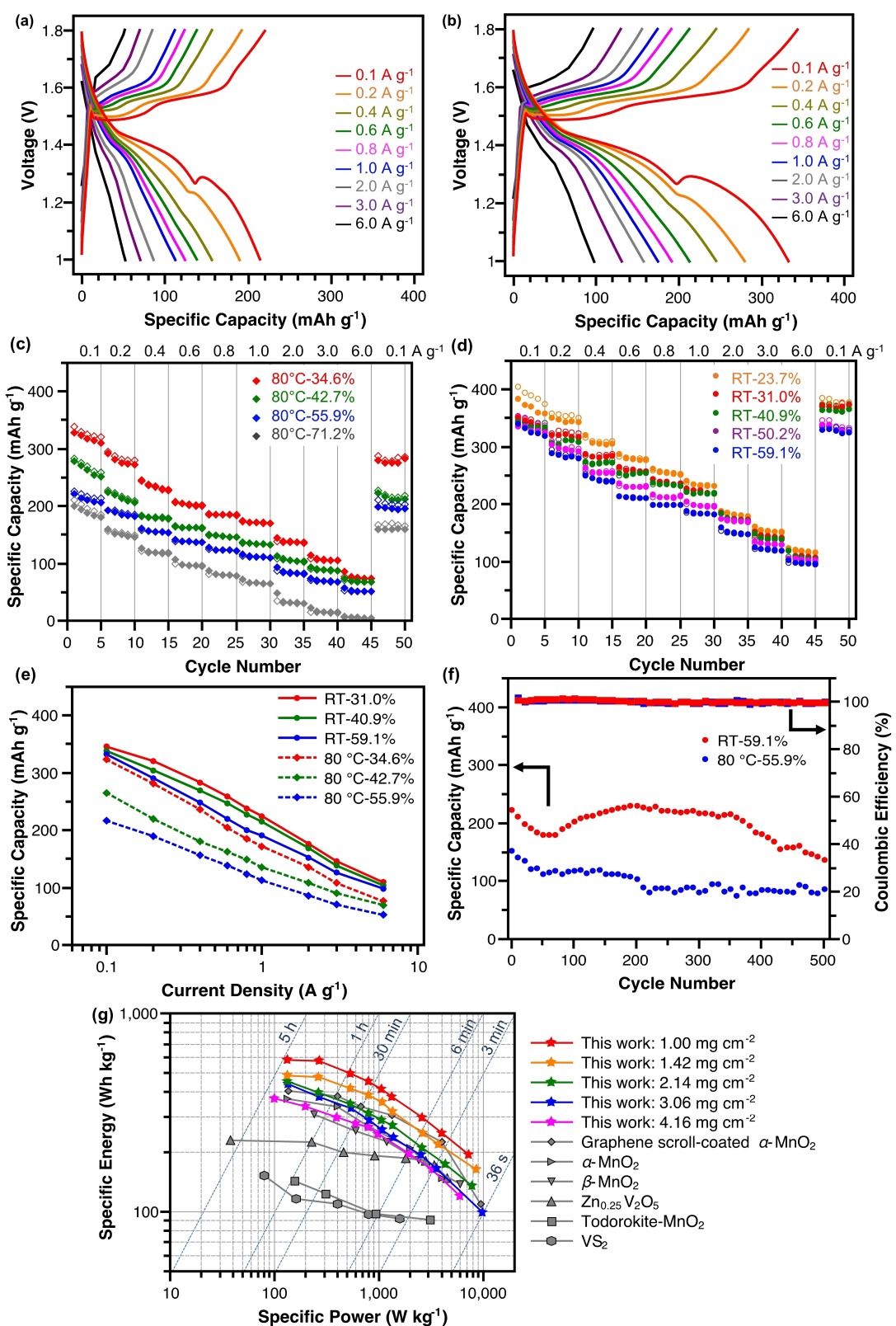


Figure 6. a, b) Charge-discharge profiles and c, d) rate capability of PCF@MnO₂ a, c) 80 °C-55.9 % and b, d) RT-59.1 % in aqueous ZIBs. e) Comparison of the specific capacity of cathodes prepared at varying temperatures with varying MnO₂ loadings. PCF@MnO₂ cathodes incubated at RT exhibited higher rate capabilities than the counterparts incubated at 80 °C at similar MnO₂ loadings. f) Cycle stability tests of both PCF@MnO₂ 80 °C-55.9 % and RT-59.1 %. g) Ragone plot of PCF@MnO₂ in comparison with other cathodes: graphene scroll-coated $\alpha\text{-MnO}_2$, $\alpha\text{-MnO}_2$, $\beta\text{-MnO}_2$, $\text{Zn}_{0.25}\text{V}_2\text{O}_5$, Todorokite-MnO₂ and VS₂. The areal MnO₂ loadings of our materials are shown.

PCF that had a large amount of uniform mesopores. RT incubation of PCF in KMnO_4 solutions promoted more uniform in-mesopore deposition of MnO_2 than high-temperature incubation. As cathodes in aqueous ZIB, PCF@ MnO_2 exhibited fast-charging capabilities, owing to the high electrical conductivity of PCF, fast ion (de-)insertion in nanometer-thick MnO_2 , and fast ion transport through the fibrous cathode. PCF@ MnO_2 reached a high loading of 59.1% of MnO_2 and showed a high capacity of 326 and 184 mAh g^{-1} at a current density of 0.1 and 1.0 A g^{-1} , respectively. This work is expected to inspire the design of fast-charging Mn-based cathodes and advance the development of high energy/power-density batteries.

Experimental Section

Chemicals

Methyl methacrylate (MMA), acrylonitrile (AN), and aluminum oxide (alumina, activated, neutral) were purchased from Sigma-Aldrich. MMA and AN were passed through an alumina-packed column chromatography to remove inhibitors before polymerizations. Cumyl dithiobenzoate (CDB), 2,2'-azobis(2-methylpropionitrile) (AIBN), benzene, dimethyl sulfoxide (DMSO), N,N-dimethylformamide (DMF), methanol, and lithium bromide (LiBr) were purchased from Sigma-Aldrich and used as received. Potassium permanganate (KMnO_4), water (HPLC grade), isopropanol, acetone, anhydrous ethanol, zinc sulfate heptahydrate ($\text{ZnSO}_4 \cdot 7\text{H}_2\text{O}$), manganese sulfate monohydrate ($\text{MnSO}_4 \cdot \text{H}_2\text{O}$), zinc foil (0.25 mm in thickness), CR2032 coin cell cases, spacers, and springs were purchased from Fisher Scientific. The CR2032 coin cell cases, spacers and springs were cleaned before use by sonicating in an isopropanol and acetone (w/w=1:1) solution for 1 h, subsequently drying at 80 °C overnight *in vacuo*. The zinc foil was cut into discs of 11 mm in diameter, then sonicated in anhydrous ethanol for 1 h. The resulting zinc discs were dried at 80 °C overnight *in vacuo* before serving as anodes. The Whatman 1823-090 glass microfiber filters (GE Healthcare Life Sciences) were cut into 19-mm-diameter discs and then used as separators. Deuterated dimethyl sulfoxide (DMSO-d₆) was purchased from Cambridge Isotope Laboratories, Inc.

Instruments

Size exclusion chromatography (SEC) was conducted on a Tosoh EcoSEC HLC-8320 equipped with a Wyatt DynaPro Nanostar light scattering detector, using DMF containing 0.05 M of LiBr as the eluent at a flow rate of 0.5 mL min^{-1} . Proton nuclear magnetic resonance (¹H NMR) spectra were collected on a 400 MHz Varian Unity in DMSO-d₆. The electrospinning was performed at a voltage of 18 kV (Acopian high voltage power supply P030HP1) and a flow rate of 0.015 $\mu\text{L min}^{-1}$ (Braintree Scientific BS-300). The distance between the syringe needle and rotating drum collector was 18 cm, and the rotational rate was 200 rpm. The oxidation and carbonization were performed in a Lindberg Blue M STF55433 C tube furnace. Nitrogen sorption was performed on a Micromeritics 3Flex Adsorption Analyzer. Scanning electron microscopy (SEM) was conducted on a LEO Zeiss 1550. The coin cells were pressed on an MTI MSK-160 E. Cyclic voltammetry was performed on a PARSTAT 4000 (Princeton Applied Research-AMETEK). The rate capabilities of zinc-ion coin cells were tested on a Neware BTS4000. X-ray diffraction (XRD) was performed on a Rigaku Miniflex 600.

Synthesis of polymer precursors for carbon fibers

PMMA-*b*-PAN with a number-average molecular weight (M_n) of 56–b-76 kDa was synthesized according to our previous report.^[45] To a 500 mL Schlenk flask equipped with a magnetic stir bar, MMA (63.8 mL), CDB (163.2 mg), AIBN (19.7 mg) and benzene (88.0 mL) were added. The solution was degassed with three freeze-pump-thaw cycles, and reacted at 65 °C for 45 h. Afterwards, the resulting pink solution was dropwise added to methanol (~1 L). The product as a pink precipitate, denoted as PMMA-CTA, was collected via vacuum filtration and dried overnight *in vacuo*. To synthesize PMMA-*b*-PAN, in a 500 mL Schlenk flask, PMMA-CTA (30444.0 mg), AN (125.6 mL), AIBN (18.5 mg) were dissolved in DMSO (340.0 mL). The resulting solution was degassed with three freeze-pump-thaw cycles, and reacted at 65 °C for 48 h. Afterwards, the viscous yellowish solution was poured into methanol (~2 L). The block copolymer product was collected via vacuum filtration, followed by drying at 70 °C overnight *in vacuo*. Besides PMMA-*b*-PAN as the precursor of porous carbon fibers (PCF), PAN homopolymer ($M_n = 140$ kDa) was synthesized to produce non-porous carbon fibers (CF). In a 500 mL Schlenk flask, AN (50.00 mL), CDB (61.2 mg), AIBN (7.4 mg), DMSO (135.00 mL) were mixed and degassed with three freeze-pump-thaw cycles, and then reacted at 65 °C for 48 h. Subsequently, the solution was added dropwise to methanol (~1 L). The PAN product was collected via vacuum filtration, followed by drying at 70 °C overnight *in vacuo*.

Preparation of porous carbon fibers

The PMMA-*b*-PAN (2.0 g) was dissolved in DMF (13 mL), and the solution was electrospun into a polymer mat (42 cm by 18 cm). The resulting polymer mats were oxidized in an air-purged tube furnace that was ramped from room temperature (RT) to 280 °C at a rate of 1 °C min⁻¹ and then kept isothermal at 280 °C for 8 h. Subsequently, the polymer mats were carbonized by ramping the temperature to 800 °C at 10 °C min⁻¹ in a nitrogen stream of 100 standard cubic centimeters per minute (sccm), and then keeping isothermal at 800 °C for 1 h. After cooling down to RT, the porous carbon fibers were collected as black mats. As a control experiment, carbon fiber (CF) mats containing no mesopores were prepared from the PAN homopolymer with the same electro-spinning and pyrolysis procedures.

Preparation of PCF@ MnO_2 cathodes

To elucidate the impact of incubation on the cathode morphology and fast-charging performance, PCF@ MnO_2 cathodes were prepared in two different KMnO_4 aqueous solutions: (i) 10 mM at 80 °C and (ii) 63 mM (1 wt%) at RT. To incubate PCF@ MnO_2 at 80 °C, KMnO_4 solutions (10 mM, 100 mL per vial, 4 vials in total) were freshly prepared in water (HPLC grade) and then set in an oil bath at 80 °C. After ~30 min for the solutions to reach an equilibrium temperature, a piece of PCF mat (100 mg) was immersed in each vial of KMnO_4 solution. The four solutions were sealed and incubated for 15, 30, 60 and 120 min, respectively. To incubate PCF@ MnO_2 at RT, fresh KMnO_4 solutions (63 mM, 100 mL per vial, 5 vials in total) were equilibrated at room temperature. Then, 100 mg of PCF mat was immersed in each vial of KMnO_4 solution. The solutions were covered and incubated for 3, 6, 12, 24 and 48 h, respectively. After incubation, all PCF@ MnO_2 mats were collected from the KMnO_4 solutions and rinsed with deionized water three times to remove any residual KMnO_4 . Afterwards, the PCF@ MnO_2 mats were dried at 80 °C overnight *in vacuo*.

Aqueous zinc-ion battery tests

The fast-charging performance was evaluated in CR2032 coin cells consisting of PCF@MnO₂ cathodes, zinc metal anodes, glass fiber separators, and aqueous electrolytes. The aqueous electrolyte contained 1 M of ZnSO₄ and 0.1 M of MnSO₄. An aliquot of 100 µL of aqueous electrolyte was added in each cell. The mass of MnO₂ in each PCF@MnO₂ cathode was ~1.4 mg. The assembled zinc-ion coin cells were tested at MnO₂-based current densities of 0.1, 0.2, 0.4, 0.6, 0.8, 1.0, 2.0, 3.0 and 6.0 A g⁻¹ between 1.80 and 1.00 volt to determine the rate capability.

Supporting Information

Supporting Information is available from the Wiley Online Library or from the author.

Acknowledgements

This material is based upon work supported by the National Science Foundation under Grant No. DMR-1752611 and the American Chemical Society Petroleum Research Foundation Doctoral New Investigator Award. The authors acknowledge the use of facilities in Nanoscale Characterization and Fabrication Laboratory (NCFL) at the Institute for Critical Technology and Applied Science (ICTAS), Virginia Tech.

Conflict of Interest

The authors declare no conflict of interest.

Data Availability Statement

The data that support the findings of this study are available from the corresponding author upon reasonable request.

Keywords: fast-charging • MnO₂-based cathodes • porous carbon fibers • zinc-ion batteries

- [1] B. Dunn, H. Kamath, J. M. Tarascon, *Science* **2011**, *334*, 928.
- [2] D. Larcher, J. M. Tarascon, *Nat. Chem.* **2015**, *7*, 19.
- [3] C. Xia, J. Guo, Y. Lei, H. Liang, C. Zhao, H. N. Alshareef, *Adv. Mater.* **2018**, *30*, 1705580.
- [4] S. Li, Y. Liu, X. Zhao, Q. Shen, W. Zhao, Q. Tan, N. Zhang, P. Li, L. Jiao, X. Qu, *Adv. Mater.* **2021**, *33*, 2007480.
- [5] D. Chao, C. R. Zhu, M. Song, P. Liang, X. Zhang, N. H. Tiep, H. Zhao, J. Wang, R. Wang, H. Zhang, H. J. Fan, *Adv. Mater.* **2018**, *30*, 1803181.
- [6] N. Zhang, F. Cheng, J. Liu, L. Wang, X. Long, X. Liu, F. Li, J. Chen, *Nat. Commun.* **2017**, *8*, 405.
- [7] W. Sun, F. Wang, B. Zhang, M. Zhang, V. Küpers, X. Ji, C. Theile, P. Bieker, K. Xu, C. Wang, M. Wenter, *Science* **2021**, *371*, 46.
- [8] H. Pan, Y. Shao, P. Yan, Y. Cheng, K. S. Han, Z. Nie, C. Wang, J. Yang, X. Li, P. Bhattacharya, K. T. Mueller, J. Liu, *Nat. Energy* **2016**, *1*, 16039.
- [9] W. Sun, F. Wang, S. Hou, C. Yang, X. Fan, Z. Ma, T. Gao, F. Han, R. Hu, M. Zhu, C. Wang, *J. Am. Chem. Soc.* **2017**, *139*, 9775.
- [10] D. Yuan, J. Zhao, H. Ren, Y. Chen, R. Chua, E. T. J. Jie, Y. Cai, E. Edison, W. Manalastas, Jr., M. W. Wong, M. Srinivasan, *Angew. Chem. Int. Ed.* **2021**, *60*, 7213.
- [11] F. Wang, E. Hu, W. Sun, T. Gao, X. Ji, X. Fan, F. Han, X.-Q. Yang, K. Xu, C. Wang, *Energy Environ. Sci.* **2018**, *11*, 3168.
- [12] M. Chen, J. Chen, W. Zhou, X. Han, Y. Yao, C. P. Wong, *Adv. Mater.* **2021**, *33*, 2007559.
- [13] J. Ding, Z. Du, B. Li, L. Wang, S. Wang, Y. Gong, S. Yang, *Adv. Mater.* **2019**, *31*, 1904369.
- [14] W. Wang, V. S. Kale, Z. Cao, Y. Lei, S. Kandambeth, G. Zou, Y. Zhu, E. Abouhamad, O. Shekhah, L. Cavallo, M. Eddaoudi, H. N. Alshareef, *Adv. Mater.* **2021**, *33*, 2103617.
- [15] Q. Tan, X. Li, B. Zhang, X. Chen, Y. Tian, H. Wan, L. Zhang, L. Miao, C. Wang, Y. Gan, J. Jiang, Y. Wang, H. Wang, *Adv. Energy Mater.* **2020**, *10*, 2001050.
- [16] S. Liu, H. Zhu, B. Zhang, G. Li, H. Zhu, Y. Ren, H. Geng, Y. Yang, Q. Liu, C. C. Li, *Adv. Mater.* **2020**, *32*, 2001113.
- [17] J. H. George Blomgren, in *Kirk-Othmer Encyclopedia of Chemical Technology*, Vol. 3, John Wiley & Sons, Inc., 2000, 434.
- [18] Y. Li, J. Fu, C. Zhong, T. Wu, Z. Chen, W. Hu, K. Amine, J. Lu, *Adv. Energy Mater.* **2018**, *9*, 1802605.
- [19] J. Shin, J. K. Seo, R. Yaylian, A. Huang, Y. S. Meng, *Int. Mater. Rev.* **2019**, *65*, 356.
- [20] L. Liu, Y. C. Wu, L. Huang, K. Liu, B. Dupoyer, P. Rozier, P. L. Taberna, P. Simon, *Adv. Energy Mater.* **2021**, *11*, 2101287.
- [21] D. Chao, C. Ye, F. Xie, W. Zhou, Q. Zhang, Q. Gu, K. Davey, L. Gu, S. Z. Qiao, *Adv. Mater.* **2020**, *32*, 2001894.
- [22] F. Y. Cheng, J. Chen, X. L. Gou, P. W. Shen, *Adv. Mater.* **2005**, *17*, 2753.
- [23] R. Yang, Y. Fan, R. Ye, Y. Tang, X. Cao, Z. Yin, Z. Zeng, *Adv. Mater.* **2021**, *33*, 2004862.
- [24] H. Pan, J. F. Ellis, X. Li, Z. Nie, H. J. Chang, D. Reed, *ACS Appl. Mater. Interfaces* **2019**, *11*, 37524.
- [25] Y. Liu, J. Zhi, M. Sedighi, M. Han, Q. Shi, Y. Wu, P. Chen, *Adv. Energy Mater.* **2020**, *10*, 2002578.
- [26] B. Wu, G. Zhang, M. Yan, T. Xiong, P. He, L. He, X. Xu, L. Mai, *Small* **2018**, *14*, 1703850.
- [27] H. Moon, K. H. Ha, Y. Park, J. Lee, M. S. Kwon, J. Lim, M. H. Lee, D. H. Kim, J. H. Choi, J. H. Choi, K. T. Lee, *Adv. Sci.* **2021**, *8*, 2003714.
- [28] Y. Jiao, L. Kang, J. Berry-Gair, K. McColl, J. Li, H. Dong, H. Jiang, R. Wang, F. Corà, D. J. L. Brett, G. He, I. P. Parkin, *J. Mater. Chem. A* **2020**, *8*, 22075.
- [29] Y. Fu, Q. Wei, G. Zhang, X. Wang, J. Zhang, Y. Hu, D. Wang, L. Zuin, T. Zhou, Y. Wu, S. Sun, *Adv. Energy Mater.* **2018**, *8*, 1801445.
- [30] S. Zhao, Y. Zuo, T. Liu, S. Zhai, Y. Dai, Z. Guo, Y. Wang, Q. He, L. Xia, C. Zhi, J. Bae, K. Wang, M. Ni, *Adv. Energy Mater.* **2021**, *11*, 2101749.
- [31] M. H. Alfaruqi, S. Islam, J. Gim, J. Song, S. Kim, D. T. Pham, J. Jo, Z. Xiu, V. Mathew, J. Kim, *Chem. Phys. Lett.* **2016**, *650*, 64.
- [32] M. H. Alfaruqi, J. Gim, S. Kim, J. Song, D. T. Pham, J. Jo, Z. Xiu, V. Mathew, J. Kim, *Electrochim. Commun.* **2015**, *60*, 121.
- [33] S. Zhu, L. Li, J. Liu, H. Wang, T. Wang, Y. Zhang, L. Zhang, R. S. Ruoff, F. Dong, *ACS Nano* **2018**, *12*, 1033.
- [34] H. T. Zhu, J. Luo, H. X. Yang, J. K. Liang, G. H. Rao, J. B. Li, Z. M. Du, *J. Phys. Chem. C* **2008**, *112*, 17089.
- [35] D. Y. Putro, M. H. Alfaruqi, S. Islam, S. Kim, S. Park, S. Lee, J.-Y. Hwang, Y.-K. Sun, J. Kim, *Electrochim. Acta* **2020**, *345*, 136189.
- [36] E. Moazzeni, E. V. Timofeeva, C. U. Segre, *J. Mater. Sci.* **2017**, *52*, 8107.
- [37] H. Xia, Y. Wang, J. Lin, L. Lu, *Nanoscale Res. Lett.* **2012**, *7*, 33.
- [38] M. Zhang, W. Wu, J. Luo, H. Zhang, J. Liu, X. Liu, Y. Yang, X. Lu, *J. Mater. Chem. A* **2020**, *8*, 11642.
- [39] J. Liu, Y. Zhang, Y. Li, J. Li, Z. Chen, H. Feng, J. Li, J. Jiang, D. Qian, *Electrochim. Acta* **2015**, *173*, 148.
- [40] Y. Jin, L. Zou, L. Liu, M. H. Engelhard, R. L. Patel, Z. Nie, K. S. Han, Y. Shao, C. Wang, J. Zhu, H. Pan, J. Liu, *Adv. Mater.* **2019**, *31*, 1900567.
- [41] Y. H. Chen, C. W. Wang, G. Liu, X. Y. Song, V. S. Battaglia, A. M. Sastry, *J. Electrochim. Soc.* **2007**, *154*, A978.
- [42] J. Chen, Y. Zhou, M. S. Islam, X. Cheng, S. A. Brown, Z. Han, A. N. Rider, C. H. Wang, *Compos. Sci. Technol.* **2021**, *209*, 108787.
- [43] C. Xie, T. Li, C. Deng, Y. Song, H. Zhang, X. Li, *Energy Environ. Sci.* **2020**, *13*, 135.
- [44] W. Qiu, Y. Li, A. You, Z. Zhang, G. Li, X. Lu, Y. Tong, *J. Mater. Chem. A* **2017**, *5*, 14838.
- [45] T. Liu, Z. Zhou, Y. Guo, D. Guo, G. Liu, *Nat. Commun.* **2019**, *10*, 675.
- [46] J. M. Serrano, T. Liu, A. U. Khan, B. Botset, B. J. Stovall, Z. Xu, D. Guo, K. Cao, X. Hao, S. Cheng, G. Liu, *Chem. Mater.* **2019**, *31*, 8898.
- [47] Z. Zhou, T. Liu, A. U. Khan, G. Liu, *Sci. Adv.* **2019**, *9*, eaau6852.

- [48] Y. Chen, Y. Zhang, D. Geng, R. Li, H. Hong, J. Chen, X. Sun, *Carbon* **2011**, *49*, 4434.
- [49] Y. Li, S. Wang, J. R. Salvador, J. Wu, B. Liu, W. Yang, J. Yang, W. Zhang, J. Liu, J. Yang, *Chem. Mater.* **2019**, *31*, 2036.
- [50] M. Chamoun, W. R. Brant, C.-W. Tai, G. Karlsson, D. Noréus, *Energy Storage Mater.* **2018**, *15*, 351.
- [51] V. Augustyn, J. Come, M. A. Lowe, J. W. Kim, P. L. Taberna, S. H. Tolbert, H. D. Abruna, P. Simon, B. Dunn, *Nat. Mater.* **2013**, *12*, 518.
- [52] P. Simon, Y. Gogotsi, B. Dunn, *Science* **2014**, *343*, 1210.
- [53] V. Augustyn, P. Simon, B. Dunn, *Energy Environ. Sci.* **2014**, *7*, 1597.
- [54] Y. Zeng, X. Zhang, Y. Meng, M. Yu, J. Yi, Y. Wu, X. Lu, Y. Tong, *Adv. Mater.* **2017**, *29*, 1700274.
- [55] D. Kundu, B. D. Adams, V. Duffort, S. H. Vajargah, L. F. Nazar, *Nat. Energy* **2016**, *1*, 16119.
- [56] J. Lee, J. B. Ju, W. I. Cho, B. W. Cho, S. H. Oh, *Electrochim. Acta* **2013**, *112*, 138.
- [57] P. He, M. Yan, G. Zhang, R. Sun, L. Chen, Q. An, L. Mai, *Adv. Energy Mater.* **2017**, *7*, 1601920.

Manuscript received: December 6, 2021

Revised manuscript received: January 14, 2022

Accepted manuscript online: January 18, 2022

Version of record online: February 3, 2022